Check for updates

Advanced Theory and Simulations

ADVANCED THEORY AND SIMULATIONS
www.advtheorysimul.com

RESEARCH ARTICLE

Single-Mn-Atom Chains Anchored on Carbon Nanotubes for Efficient Naphthalene Hydrocracking

Changsheng Hou[1] | Yiheng Shen[2] | Wu Su[3] | Zichang Zhang[1] | Wei Sun[1] | Xiaobing Kong[1] | Anyuan Cao[1] | Yuansheng Zhao[3] | Qian Wang[1]

[1]School of Materials Science and Engineering, Peking University, Beijing, China | [2]Materials Genome Institute, Shanghai University, Shanghai, China | [3]Petrochemical Research Institute, PetroChina Company Limited, Beijing, China

Correspondence: Anyuan Cao (anyuan@pku.edu.cn) | Yuansheng Zhao (zhaoyuansheng@petrochina.com.cn) | Qian Wang (qianwang2@pku.edu.cn)

Received: 8 September 2025 | **Revised:** 2 December 2025 | **Accepted:** 4 December 2025

Keywords: bifunctional catalysts | carbon nanotube sponges | first-principles calculations | polyaromatics hydrocracking | single-metal-atom chains

ABSTRACT

The design of efficient catalysts with high atomic utilization is crucial for effective conversion of polycyclic aromatic hydrocarbons (PAHs) in heavy oil of petroleum. Inspired by recent experimental advances in the successful synthesis of single-metal-atom chains confined within 2D semiconductors [*Nat. Commun*. 2025, 16, 4924], we design a series of single metal atoms arranged along nanoscale substrates as space-tunable single-metal-atom chain catalysts for heavy oil hydrocracking. Using naphthalene as a prototypical PAH, we perform first-principles calculations combined with rational screening over transition metal series (TM = Ti, V, Cr, Mn, Fe, Co, Ni, Cu, Zn, Zr, Nb, Mo, W) to identify the most promising candidate of single atom chains anchored on CNTs(n, n) (n = 4, 6, 8, 10). Our results show that MnN_4@CNT(8, 8) emerges as the most promising candidate for a high-performance catalyst, demonstrating excellent hydrogenation activity with a low energy barrier of 1.47 eV for the rate-determining step ($2\beta \rightarrow 3\beta$), as well as efficient C—C bond cleavage in tetralin with an energy barrier of 1.92 eV. This work demonstrates the potential of single-metal-atom chains as superior catalysts for heavy oil hydrocracking.

1 | Introduction

With the increasing prevalence of heavy fractions in crude oil reserves, extensive research efforts have been devoted to developing advanced heavy oil upgrading technologies to enable high-value utilization of these inferior feedstocks [1]. Among various refining technologies, catalytic hydrocracking has emerged as one of the most efficient processes for converting polycyclic aromatic hydrocarbons (PAHs) into valuable light chemicals such as methane, ethylene, benzene, toluene, ethylbenzene, and xylene (BTEX) through selective C—C bond cleavage under hydrogen atmosphere at high temperature and pressure [2–4]. Theoretically, the hydrocracking reaction can be considered as a combined hydrogenation and catalytic cracking process. Hydrogenation, catalyzed by metal active sites, saturates reactant bonds and facilitates subsequent cracking. Meanwhile, acid sites commonly exist in zeolites promote the decomposition of complex aromatic rings and long-chain structures into smaller, simple molecules. Industrial hydrocracking relies on bifunctional catalysts, typically consisting of hydrogenation catalysts supported on large-pore zeolites [5]. The Brønsted acidic sites (BAS) in zeolites facilitate cracking [6], while active metals (e.g., Ni, Mo, Pt) in hydrogenation catalysts play a crucial role in hydrogenation [7]. However, achieving fine dispersion of metal catalysts on zeolite supports demands complex and challenging catalyst synthesis, and the detailed mechanisms underlying PAH hydrocracking on such catalysts remain poorly understood [8–11].

In recent years, single-atom catalysts (SACs) have gained increasing attention due to their exceptional activity, selectivity, and

© 2025 Wiley-VCH GmbH

stability [12–14]. SACs offer enhanced atomic efficiency because of the highly unsaturated coordination environment and the strong metal–support interaction [15, 16]. Moreover, the well-defined single-atom structure of SACs provides a simplified model for mechanistic study, which is particularly advantageous for elucidating the hydrocracking mechanism of PAHs [4]. Additionally, SACs also exhibit excellent hydrogenation performance, and the activation of H_2 plays a critical role in PAHs hydrocracking process [12]. The carbon nanotube sponges with high specific surface area have good oil dispersion and also can greatly inhibit coking during PAHs hydrocracking process [17]. Previous studies have been verified that the carbon-supported single-atom Mo catalyst and MoCo dual-atomic site catalyst can activate hydrogen and promote efficient conversion of heavy oil in the slurry hydrogenation of heavy oil [18, 19]. However, the limited number of active sites in single-atom catalysts poses a significant challenge, which substantially restricts further improvement of the hydrocracking efficiency for heavy oil. This intrinsic limitation stems from the isolated nature of single-atom configurations, where each metal atom functions as an individual active center. Consequently, the relatively low density of these atomic-scale active sites becomes a bottleneck for achieving optimal catalytic performance in complex hydrocarbon conversion processes.

Recently, the experimental realization of single-metal-atom chains (SMACs) provides a promising solution to secure increased density of atom catalysts with tunable distribution by using 1D arrays of catalytically active metal centers [20]. Besides, previous DFT studies have shown that transition-metal strings templated on boron-doped carbon nanotubes exhibit distinct electronic properties, highlighting their promise for nanocatalysis [21]. In this study, we systematically investigate the stability of SMACs anchored on carbon nanotubes (CNTs) with varying diameters and evaluate their hydrocracking performance, using naphthalene as a representative PAH molecule, based on first-principles calculations combined with a comprehensive screening strategy. Our study on the application of SMACs in hydrocracking of PAHs may provide theoretical insights for the experimental synthesis of SMACs-based hydrocracking catalysts.

2 | Results and Discussion

As shown in Figure 1a, we rationally design a screening procedure for systematically identifying high-performance, cost-effective SMACs as superior catalysts for heavy oil hydrocracking with significantly improved active site characteristics compared to conventional SACs. The screening criteria prioritize experimentally feasible SACs composed of abundant transition metals (TMs) with price < 100 USD/kg, ultimately selecting 13 candidate metals (TM = Ti, V, Cr, Mn, Fe, Co, Ni, Cu, Zn, Zr, Nb, Mo, W) for detailed investigation, as shown in Figure 1b. Each TM atom in SMACs is anchored through a tetravalent nitrogen coordination motif (TMN_4), forming a well-defined TMN_4@CNT(8, 8) crystal structure where the SMACs are epitaxial embedded within the armchair (8, 8) CNT, as displayed in Figure 1c. The (8, 8) chirality is specifically chosen for two key reasons: First, as a metallic armchair CNT, it can enhance charge delocalization along the SMACs, thus promoting catalytic activity. Second, CNT(8, 8) was found to possess the most favorable metal–support interaction energy compared to other chirality [22]. The combination of metallicity and optimized metal–support interaction synergistically stabilizes the SMACs and promotes efficient electron transfer during catalytic reaction. After full geometry optimization, the unit cells of TMN_4@CNT(8, 8) (TM = Ti, V, Cr, Mn, Fe, Co, Ni, Mo, W) remain almost intact, while the other four configurations (TM = Cu, Zn, Zr, Nb) completely collapse, indicating unstable hybrid structures made from these four metals. The subsequent screening process then focuses exclusively on the nine stable structures.

The activation of H_2 plays a critical role in the hydrocracking process of PAHs [12]. Our calculations reveal that among the screened TMN_4@CNT(8, 8) (TM = Ti, V, Cr, Mn, Fe, Co, Ni, Mo, W), the three structures with TM = Mn, Cr, and Fe exhibit relatively low H_2 dissociation energy ($E_{H\text{-}H}$), which is 1.89, 2.57, and 2.73 eV, respectively, as presented in Table S1. We also find that these SMACs consisting of low-cost transition metals (Mn, Cr, Fe) anchored on the CNT(8, 8) exhibit superior H_2 activation capability compared to some noble-metal-based systems [PtN_4@CNT(8, 8): 3.13 eV; RhN_4@CNT(8, 8): 3.14 eV; PdN_4@CNT(8, 8): 3.61 eV], highlighting the economic advantages for hydrocracking catalysis, as demonstrated in Figure 2a,b. The low dissociation energy observed originates from the physisorption of H_2 molecule and chemisorption of atomic H on TMN_4@CNT(8, 8). The deformation charge densities in Figure 2c show distinct charge redistribution patterns, with the yellow and blue regions representing electron accumulation and depletion, respectively. In the case of H_2 molecule, we observe only minor charge perturbation, indicating weak interactions. In contrast, the adsorption of atomic H results in pronounced charge redistribution, reflecting a stronger interaction with the surface. Bader charge analysis further reveals that the adsorption of H atom involves mixed covalent–ionic bonding with the substrate, with a much stronger covalent character on MnN_4@CNT(8, 8), different from the weak physisorption of H_2 molecule. Moreover, the *d*-band center of CrN_4@CNT(8, 8) (–0.537 eV) is found to be closer to the Fermi level than those of MnN_4@CNT(8, 8) (–0.789 eV) and FeN_4@CNT(8, 8) (–1.173 eV), suggesting a stronger adsorption capability on the CrN_4 site, as illustrated in Figure 2d.

We then calculate the adsorption energies (E_{ads}) of molecular H_2, atomic H, naphthalene, and tetralin on TMN_4@CNT(8, 8) (TM = Cr, Mn, Fe). The results are summarized in Table 1, showing that the absolute values of $E_{ads}(H_2)$ and $E_{ads}(H)$ exhibit a trend of CrN_4 > MnN_4 > FeN_4, in excellent agreement with the *d*-band center positions. Specifically, the Cr site in CrN_4@CNT(8, 8) possesses the strongest adsorption capability with E_{ads} of –0.86 eV for H_2 and –2.82 for H, followed by MnN_4 (–0.08 eV for H_2 and –2.71 for H) and FeN_4 (–0.07 eV for H_2 and –1.86 for H). Such correlation between the *d*-band center positions and adsorption strengths of small molecules confirms that the higher-lying *d*-band facilitates stronger interaction with adsorbates through enhanced orbital hybridization. Notably, the E_{ads} of PAHs reveal distinct characteristics among these three catalytic systems. As shown in Table 1, CrN_4@CNT(8, 8) exhibits excessively strong naphthalene adsorption [$E_{ads}(C_{10}H_8)$ = –2.45 eV], which could compete with adsorption of hydrogen and consequently hinder the hydrogenation process. This competitive adsorption effect makes CrN_4@CNT(8, 8) unsuitable as a candidate for hydrogenation process from naphthalene to tetralin. The optimized config-

25130390, 2026, 3, Downloaded from https://advanced.onlinelibrary.wiley.com/doi/10.1002/adts.202501713 by Peking University, Wiley Online Library on [03/04/2026]. See the Terms and Conditions (https://onlinelibrary.wiley.com/terms-and-conditions) on Wiley Online Library for rules of use; OA articles are governed by the applicable Creative Commons License

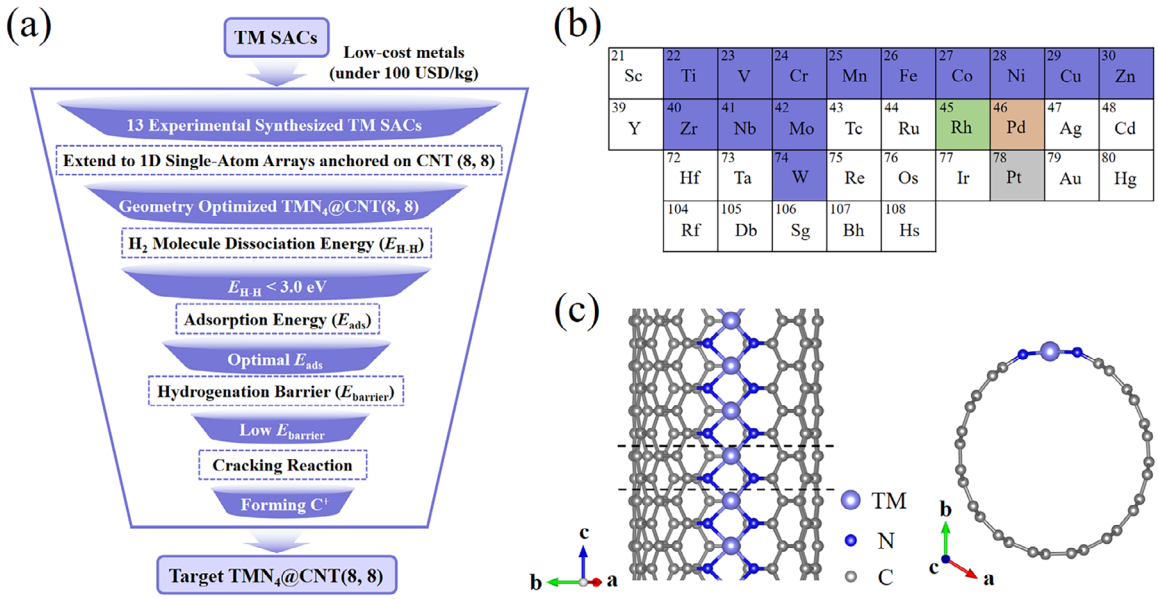

FIGURE 1 | (a) Schematic of the screening procedures for the single-atom chains anchored on CNT (8, 8). (b) Periodic table highlighting transition metals screened for SACs: purple denotes low-cost metals, while other colors represent excluded expensive metals. (c) Schematic illustration of the TMN_4@CNT(8, 8) crystal structure.

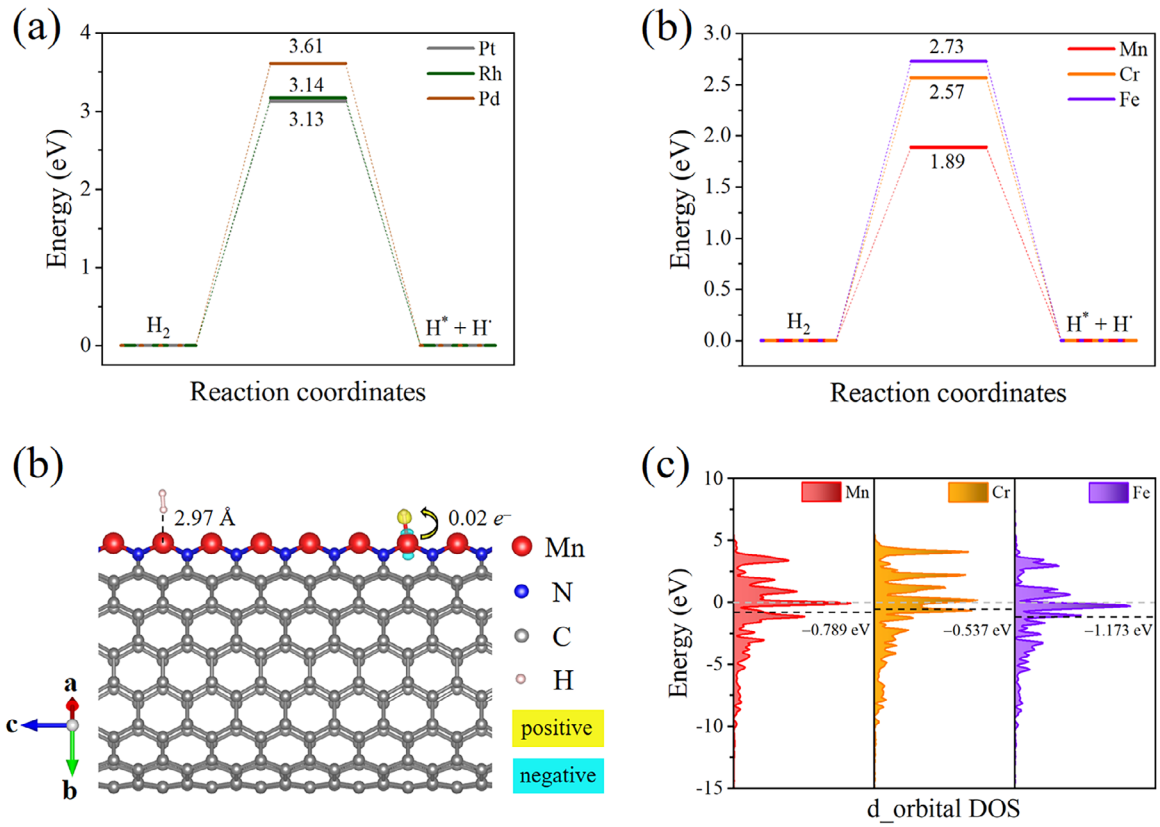

FIGURE 2 | (a, b) Schematic illustration of H_2 dissociation on TMN_4@CNT(8, 8). (c) Spatial distribution of the deformation charge density and Bader charge analysis for H_2 molecule and H atom adsorption on MnN_4@CNT(8, 8). The yellow and blue regions represent charge accumulation and depletion, respectively, and the isosurface values are ± 0.03 $Å^{-3}$. (d) *d*-band center of TMN_4@CNT(8, 8) (TM = Mn, Cr, Fe).

25130390, 2026, 3, Downloaded from https://advanced.onlinelibrary.wiley.com/doi/10.1002/adts.202501713 by Peking University, Wiley Online Library on [03/04/2026]. See the Terms and Conditions (https://onlinelibrary.wiley.com/terms-and-conditions) on Wiley Online Library for rules of use; OA articles are governed by the applicable Creative Commons License

TABLE 1 | Adsorption energies E_{ads} (in eV) of H_2 molecule, H atom, naphthalene ($C_{10}H_8$), and tetralin ($C_{10}H_{12}$) on TMN_4@CNT(8, 8).

TMN_4@CNT(8, 8)	E_{ads} (H_2)	E_{ads} (H)	E_{ads} ($C_{10}H_8$)	E_{ads} ($C_{10}H_{12}$)
Mn	−0.08	−2.71	−0.26	−1.11
Fe	−0.07	−1.86	−0.45	−0.38
Cr	−0.86	−2.82	−2.45	−1.80

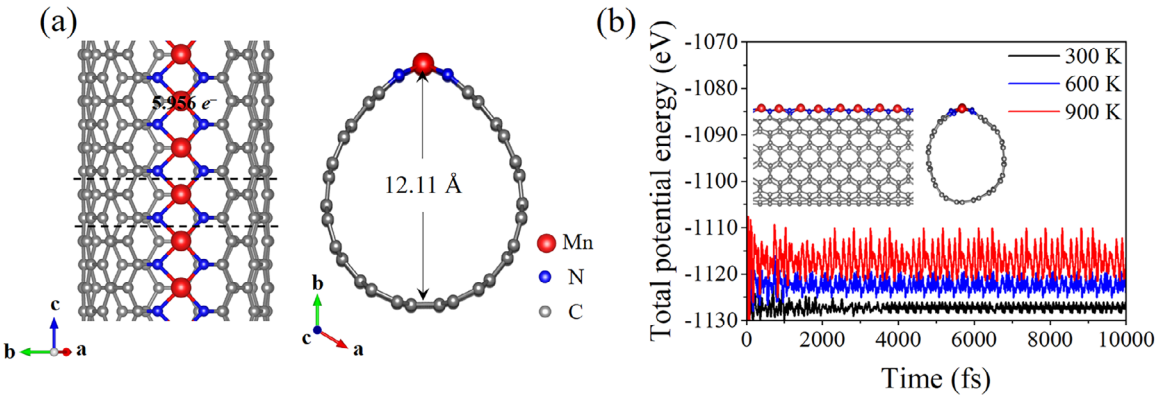

FIGURE 3 | (a) Geometry and Bader charge of the MnN_4@CNT(8, 8) crystal structure. The unit cell is indicated by dashed lines. (b) Variation of the total potential energy with simulation time for MnN_4@CNT(8, 8) during the AIMD simulation at 300, 600, and 900 K. The inset is the supercell at the end of the simulation at 900 K.

urations of naphthalene and tetralin adsorbed on TMN_4@CNT(8, 8) (TM = Cr, Mn, Fe) are presented in Figure S1. More importantly, the tetralin molecule adsorbed on FeN_4@CNT(8, 8) exhibits negligible structural distortion, indicating insufficient activation of the C—C bonds for subsequent cracking reactions. Such observation correlates well with its relatively weak adsorption energy for tetralin on FeN_4@CNT(8, 8) [$E_{ads}(C_{10}H_{12}) = -0.38$ eV], compared to −1.11 eV on MnN_4@CNT(8, 8) and −1.80 eV on CrN_4@CNT(8, 8), as quantified in Table 1. The low adsorption energy and lack of tetralin activation suggest that FeN_4@CNT(8, 8) cannot effectively facilitate the tetralin cracking process. Consequently, both CrN_4@CNT(8, 8) and FeN_4@CNT(8, 8) are excluded from further consideration, leaving MnN_4@CNT(8, 8) as the most promising candidate for subsequent investigations of PAHs hydrocracking reactions. To clarify the electronic role of the CNT support, we perform comparative Bader charge analysis in Figure S2. For an isolated Mn chain, the Mn atom retains a valence electron of 7 e^-, showing no charge transfer and no acidic character. In contrast, within the MnN_4@CNT(8, 8) system, the Mn valence electron decreases to 5.956 e^-, while the N atoms increase to 6.075 e^-. This pronounced electron transfer from Mn to the N-doped CNT support creates a strong acid site on the Mn center, which is essential for activating the tetralin cracking reaction.

The optimized structure of MnN_4@CNT(8, 8) is given in Figure 3a, which has a lattice constant of c = 2.47 Å and a maximum diameter of 12.11 Å with a symmetry of *P*m (space group no. 6), containing 1 Mn atom, 2 N atoms, and 28 C atoms in its primitive cell. Bader charge analysis [23, 24] reveals that significant charge transfer occurs from the Mn atoms to the substrate, reducing the valence electron of Mn to 5.956. Such electron-deficient state activates Mn as acid center, which subsequently functions as the active site for catalytic cracking reactions.

To check the thermal stability of MnN_4@CNT(8, 8), we perform AIMD simulations from 300 to 900 K with a temperature interval of 300 K. A 1 × 1 × 8 supercell is used to reduce the fake stability resulted from the periodic boundary conditions and the simulation time is set to be 10 *p*s with a time step of 1 *f*s for all the simulations. The results at 900 K are plotted in Figure 3b, which shows that the geometric skeleton of MnN_4@CNT(8, 8) remains its structural integrity throughout the simulation, and the total potential energy fluctuates slightly around a static value during the whole process, suggesting that MnN_4@CNT(8, 8) is thermally stable even at high temperature of 900 K. To improve the clarity of the energy fluctuations at 300 K, a zoomed-in view of the total potential energy trajectory is provided in Figure S3.

To examine the magnetic coupling of Mn atoms in the chain, we carry out calculations for the ferromagnetic (FM), antiferromagnetic (AFM), ferrimagnetic (FIM), and non-spin-polarized (NSP) states, in a total of 10 configurations, as presented in Figure S4. We find that all the atomic magnetic moments of the FIMs and AFM states vanish after geometry optimization, while the FM configuration is metastable as compared to the ground NSP state, suggesting that MnN_4@CNT(8, 8) is non-magnetic.

Next, we study the entire hydrogenation process from naphthalene to tetralin on MnN_4@CNT(8, 8) in detail. Considering the geometric and electronic structure of naphthalene, there are 12 possible hydrogenation routes, as shown in Figure 4a. At the beginning of hydrogenation, according to the geometric symmetry and uneven charge distribution between the α- and β-site electron cloud densities, the first step would occur on

25130390, 2026, 3, Downloaded from https://advanced.onlinelibrary.wiley.com/doi/10.1002/adts.202501713 by Peking University, Wiley Online Library on [03/04/2026]. See the Terms and Conditions (https://onlinelibrary.wiley.com/terms-and-conditions) on Wiley Online Library for rules of use; OA articles are governed by the applicable Creative Commons License

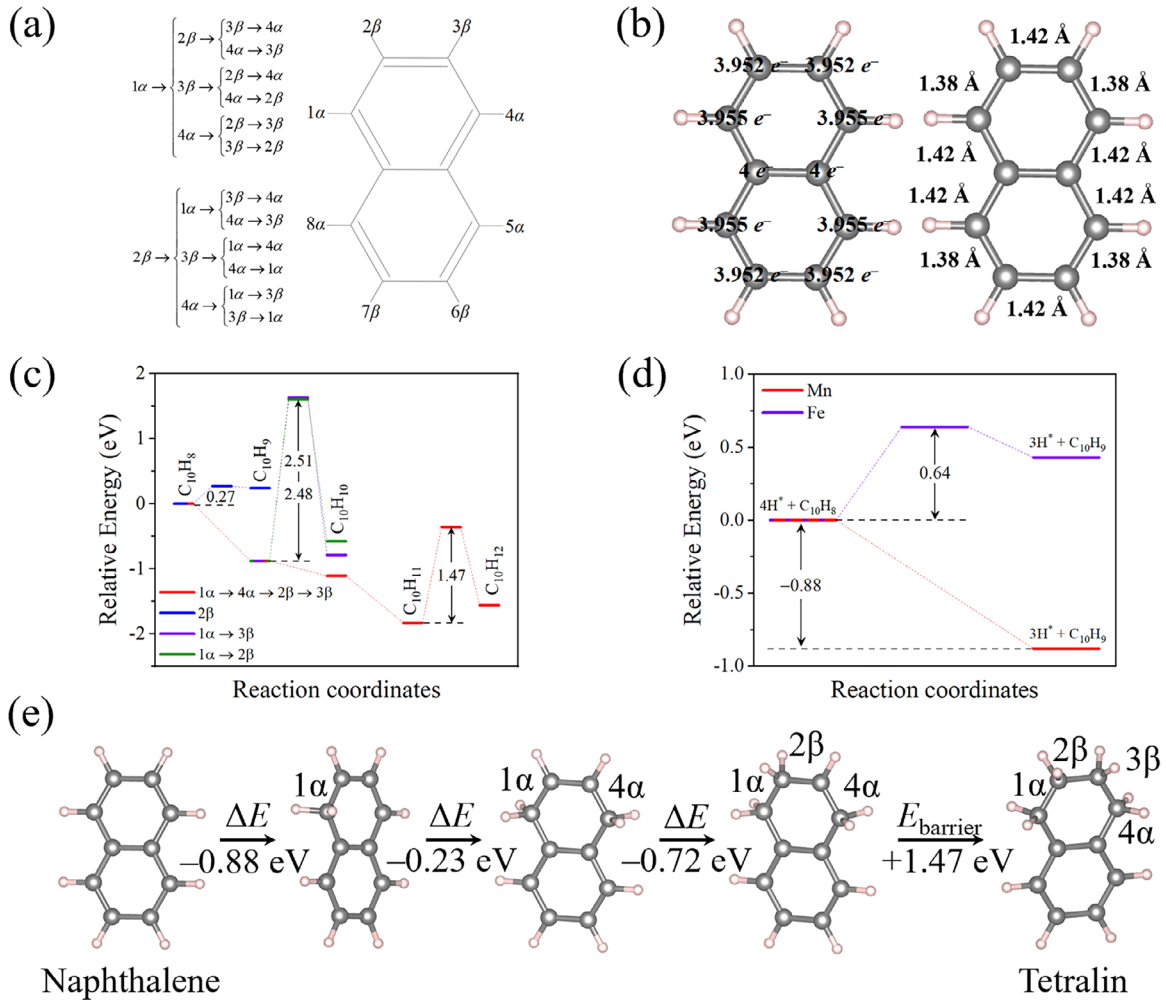

FIGURE 4 | Identification of optimal hydrogenation path from naphthalene to tetralin. (a) All potential hydrogenation sequences and corresponding hydrogenation sites. (b) Charge distribution and bond lengths in naphthalene. (c) Hydrogenation energy step graph from naphthalene to tetralin on MnN_4@CNT(8, 8). The red lines for the optimal steps. (d) Hydrogenation energy started step graph of naphthalene on FeN_4@CNT(8, 8) and MnN_4@CNT(8, 8), respectively. (e) Detailed procedure for the hydrogenation of naphthalene into tetralin on MnN_4@CNT(8, 8).

either the α- or β-site in one of the benzene rings. As shown in Figure 4b, the naphthalene molecule exhibits symmetric bond length (1.38–1.42 Å), while Hirshfeld charge analysis [25] reveals slight electronic asymmetry between the α- and β-sites, with α-carbons possessing more electrons than β-carbons, indicating preferential initial hydrogenation reactivity at the α-site due to its denser electron density. We then calculate and compare the performance of all the representative paths in terms of energy step diagram in Figure 4c. We find that the initiating hydrogenation step at the α-site is barrierless, which prevails over that at the β-site with an activation energy of 0.27 eV, in consistence with our Hirshfeld charge analysis. Thus, we exclude the six pathways starting from the β-site. By considering the catalytic energy barrier and overall energy change, we identify the optimal hydrogenation pathway: $1\alpha \rightarrow 4\alpha \rightarrow 2\beta \rightarrow 3\beta$, where the final step ($3\beta$-site) is the rate-determining step with an energy barrier of 1.47 eV. For comparison, other paths are hindered by the high barrier of over 2.4 eV at the second step. Notably, the first three steps in the optimal pathway (1α, 4α, 2β-sites) are barrierless, and thus spontaneous. The initial α-site hydrogenation proceeds barrierlessly on MnN_4@CNT(8, 8), while an energy barrier of 0.64 eV is required on FeN_4@CNT(8, 8) (Figure 4d). For the optimal pathway ($1\alpha \rightarrow 4\alpha \rightarrow 2\beta \rightarrow 3\beta$), MnN_4@CNT(8, 8) exhibits a lower rate-determining step barrier of 1.47 eV compared to 2.33 eV for FeN_4@CNT(8, 8) (Figure S5), showing the superior catalytic activity of MnN_4@CNT(8, 8) for naphthalene hydrogenation. The complete hydrogenation pathway from naphthalene to tetralin on MnN_4@CNT(8, 8) with stepwise energy profile is schematically illustrated in Figure 4e. Such progressive saturation mechanism effectively converts the aromatic naphthalene into fully hydrogenated tetralin while maintaining the structural integrity of the MnN_4 catalytic center.

To study the cracking mechanism of tetralin on MnN_4@CNT(8, 8), we systematically analyze both the bond length and Hirshfeld charge distribution of the adsorbed tetralin molecule (Figure 5a). The asymmetric charge distribution in such a symmetrical molecule arises from the influence of the cracking catalytic substrate. We find significant electron depletion for the four hydrogenated carbon atoms in tetralin, where the four hydrogenated carbon atoms tend to form carbonium ions (C^+) when tetralin molecules contact with the acidic centers on MnN_4@CNT(8, 8). The strong Coulomb repulsion between

25130390, 2026, 3, Downloaded from https://advanced.onlinelibrary.wiley.com/doi/10.1002/adts.202501713 by Peking University, Wiley Online Library on [03/04/2026]. See the Terms and Conditions (https://onlinelibrary.wiley.com/terms-and-conditions) on Wiley Online Library for rules of use; OA articles are governed by the applicable Creative Commons License

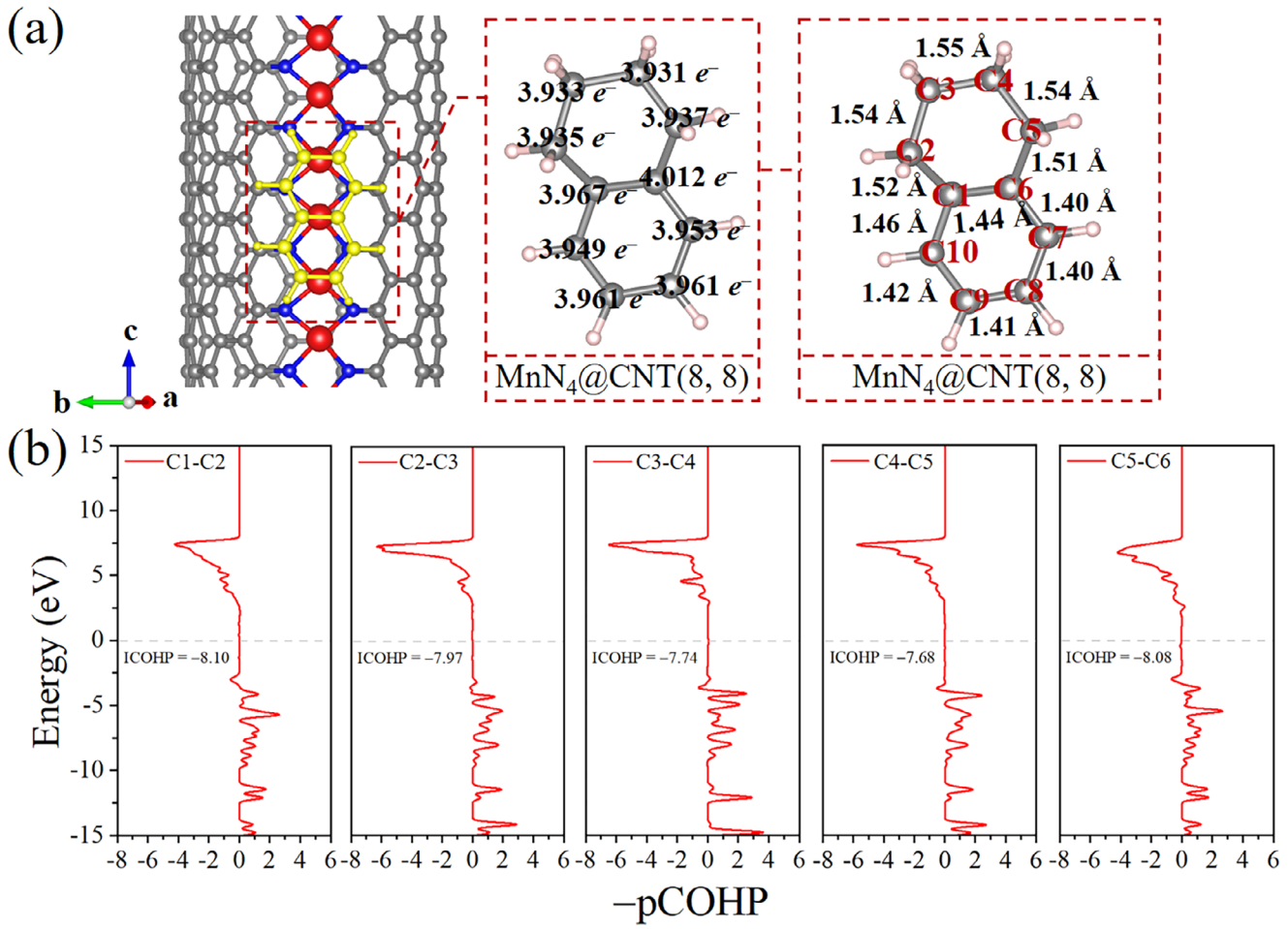

FIGURE 5 | (a) Charge distribution and bond length of the adsorbed tetralin on MnN_4@CNT(8, 8). (b) Crystal orbital Hamilton population (COHP) of the C—C bonds of tetralin adsorption on MnN_4@CNT(8, 8). The adsorbates are highlighted in yellow for clarity.

the C^+ weakens the strength of the bond. The bond length analysis of carbon atoms also suggests the feasibility of bond breaking where the C—C bonds involving C^+ in the cyclohexane ring display an average length of 1.53 Å, exceeding the 1.42 Å average bond length observed for the non-hydrogenated carbons in the benzene ring, indicating greater bond weakening and enhanced cleavage susceptibility for hydrogenated positions. To further study the bonding strength between the C atoms in the tetralin adsorbed on MnN_4@CNT(8, 8), we perform projected COHP calculations, where the positive portion of the curve represents the bonding contribution and the negative portion corresponds to the antibonding contribution. The integral value of the COHP curve (ICOHP) can be interpreted as the number of bonded electrons shared by two C atoms, and a larger absolute value implies a stronger bond strength. In the tetralin/MnN_4@CNT(8, 8) system, the absolute ICOHP values for the bonds formed by hydrogenated carbons (Figure 5b) are significantly smaller than those by totally non-hydrogenated carbons (Figure S6), leading to a weaker bonding of hydrogenated C^+ centers. This result agrees well with previous Hirshfeld charge and bond length analyses. Among all the bonds in the adsorbed tetralin, the fully hydrogenated C—C bonds (C2—C3, C3—C4, and C4—C5) exhibit the lowest ICOHP values, indicating they are most prone to cleavage during tetralin cracking process.

To investigate the main cracking products of tetralin on MnN_4@CNT(8, 8), we examine the highlighted easy-to-break bonds (C3—C4, C4—C5, C5—C6) in Figure 6a based on the geometric symmetry of tetralin molecule. Our calculated results reveal that the cleavage barriers are distinct with the values of 2.30 eV (C3—C4), 1.92 eV (C4—C5), and 3.31 eV (C5—C6), as given in Figure 6b, suggesting that the C4—C5 bond breaks most easily, consistent with the above COHP analysis. As shown in Figure S7, we analyze the Mn—N bonding characteristics during both the hydrogenation and C—C cracking steps using bond-length monitoring and −pCOHP analysis. The Mn—N bonds undergo only minor elongation (≤ 0.03 Å) and show no appreciable loss of bonding strength, even at transition states where the energy barrier reaches 1.92 eV. These findings indicate that the Mn center remains firmly anchored to the substrate and structurally stable throughout the catalytic cycle. Furthermore, Bader charge analysis along the reaction pathway (Figure S8) reveals only negligible fluctuations in the Mn atom's charge state. This minimal variation in electron density further corroborates the structural and electronic stability of the Mn site during catalysis. Synergistically, these results indicate that the high reaction barrier originates from the intrinsic kinetics of the substrate transformation, rather than from any destabilization or weakening of the Mn active site. As shown in Table 2, we calculate the bond strength of C3—C4, C4—C5, and C5—C6 bonds

25130390, 2026, 3, Downloaded from https://advanced.onlinelibrary.wiley.com/doi/10.1002/adts.202501713 by Peking University, Wiley Online Library on [03/04/2026]. See the Terms and Conditions (https://onlinelibrary.wiley.com/terms-and-conditions) on Wiley Online Library for rules of use; OA articles are governed by the applicable Creative Commons License

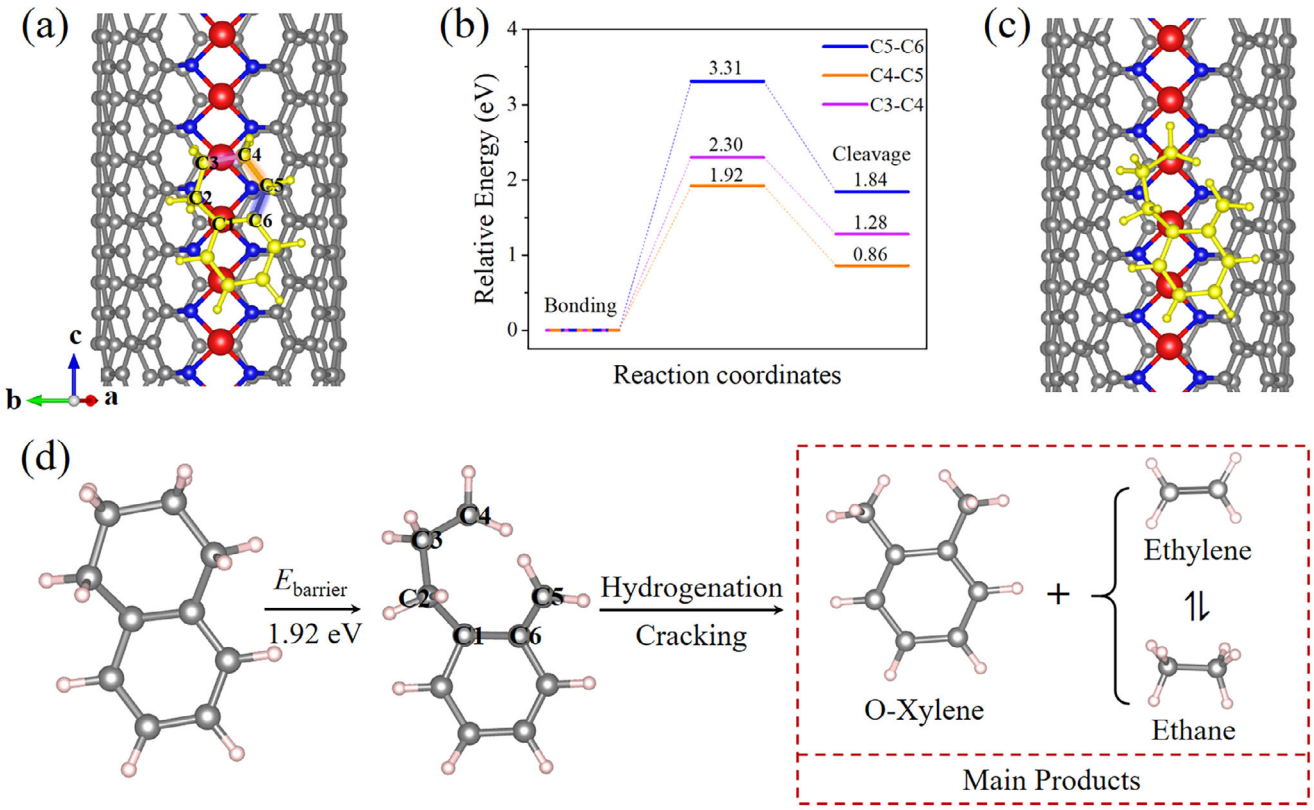

FIGURE 6 | Cracking process of tetralin and main products. (a) Highlighted bonds in the tetralin adsorbed on MnN_4@CNT(8, 8). (b) Cracking energy step graph of tetralin. (c) Schematic illustration of the C4—C5 bond cleavage in tetralin adsorption on MnN_4@CNT(8, 8). (d) Schematic diagram of the cracking process of tetralin and its main products. The adsorbates are highlighted in yellow for clarity.

TABLE 2 | Calculated C—C bond binding energy E_b (in eV) of the tetralin adsorbed on MnN_4@CNT(8, 8) or in free-standing state.

Bond Types	E_b (on MnN_4@CNT(8, 8))	E_b (free-standing state)
C3-C4	1.28	2.00
C4-C5	0.86	3.04
C5-C6	1.84	5.07

in tetralin both with and without MnN_4@CNT(8, 8) catalyst, and find that the catalyst significantly reduces the C—C bonding and significantly promotes the cracking reactions of tetralin. Figure 6c presents the optimized structure after C4—C5 bond cleavage, confirming the preferential cracking pathway. Figure S9 shows the COHP analysis of remaining bonds after C4—C5 bond cleavage in tetralin adsorbed on MnN_4@CNT(8, 8), revealing that the C2—C3 bond with smaller ICOHP absolute value becomes more susceptible to subsequent cleavage. Figure 6d illustrates the cracking process, where the C4—C5 bond cleavage with a 1.92 eV barrier is followed by preferential C2—C3 bond breaking to form ethylene and 1,2-dihydro-O-Xylene (C_8H_8). Under hydrogen atmosphere at high temperature and pressure, the unsaturated C2 and C5 sites could undergo further hydrogenation to produce O-Xylene (C_8H_{10}), while ethylene and ethane could reach a reversible equilibrium. Based on above discussion, we conclude that naphthalene hydrogenation on MnN_4@CNT(8, 8) forms tetralin, which subsequently cracks into O-Xylene, ethylene, and ethane as main products.

Next, we examine the effects of Mn loading amount and CNT diameters on naphthalene hydrogenation and tetralin cracking reactions. The MnN_4@CNT(8, 8) −100%, −50%, and −33% represent the Mn loading amount in the studied configurations, as shown in Figure S10. Bader charge analysis shows the number of valence electrons of Mn changing with the loading amount as 5.956 (100%), 6.125 (50%), and 6.274 (33%), implying the tunable acidity and cracking activity. As shown in Table S2, the calculated formation energies (E_f) of MnN_4@CNT(8, 8) with different Mn loading amount of 100%, 50%, 33% are –0.06 –0.08, and –0.07 eV/atom, respectively, implying that the formation from the constituent elements is exothermic and energetically favorable. Subsequent investigations focus on hydrogenation and cracking performance across these three configurations. Figure S11 shows that as the anchored Mn content increases in MnN_4@CNT(8, 8), the energy barrier for the hydrogenation rate-determining step ($2\beta \rightarrow 3\beta$) decreases significantly from 2.38 eV (33%) to 1.85 eV (50%) and further to 1.47 eV (100%), indicating that MnN_4@CNT(8, 8)-100% exhibits the most efficient hydrogenation

25130390, 2026, 3, Downloaded from https://advanced.onlinelibrary.wiley.com/doi/10.1002/adts.202501713 by Peking University, Wiley Online Library on [03/04/2026]. See the Terms and Conditions (https://onlinelibrary.wiley.com/terms-and-conditions) on Wiley Online Library for rules of use; OA articles are governed by the applicable Creative Commons License

performance compared to the lower Mn-loading configurations, and the C4-C5 bond is most susceptible to cleavage in tetralin adsorbed on MnN_4@CNT(8, 8). Further investigation of Mn loading effects reveals that C4—C5 bonding strength varies with Mn loading as 0.85 eV (100%), 1.93 eV (50%), and 2.75 eV (33%) as listed in Table S3, implying the enhanced cracking activity with high anchored Mn content, which aligns perfectly with the Bader charge analysis that shows greater acidity at higher Mn loadings. Figure S12 presents the optimized structural configurations following C4—C5 bond cleavage in tetralin adsorbed on MnN_4@CNT(8, 8) with different fractions of anchored Mn atoms (100%, 50%, and 33%), clearly demonstrating the structural evolution during the cracking process across different catalyst compositions.

To explore the curvature effect of CNTs on catalytic activity, we anchor Mn single-atom chains on CNTs(n, n) (n = 4, 6, 8, 10) and graphene, forming MnN_4@CNT(n, n) and MnN_4@graphene systems, where graphene approximates CNTs with an extremely low curvature. Bader charge analysis of Mn valence electrons in these structures (Figure S13) reveals that MnN_4@CNT(8, 8) has the smallest valence electron (5.956 e^-) on Mn sites, indicating the strongest acidity of MnN_4 centers compared to other configurations. As shown in Table S4, the calculated E_f of MnN_4@CNTs(n, n) and MnN_4@graphene systems depend on the substrate curvature. The E_f value decreases from 0.26 eV/atom for the high-curvature CNT (4, 4) to –0.09 eV/atom for flat graphene, indicating enhanced thermodynamic stability with reduced curvature. The energy barrier for the hydrogenation rate-determining step ($2\beta \rightarrow 3\beta$) exhibits a non-linear dependence on CNTs curvature, as shown in Figure S14. The lowest barrier (1.47 eV) is found in MnN_4@CNT(8, 8), while the systems with larger [MnN_4@CNT(4, 4) and MnN_4@CNT(6, 6)] and lower [MnN_4@CNT(10, 10) and MnN_4@graphene] curvatures all exhibit larger barriers (1.55–3.12 eV), indicating that optimal curvature is essential for maximizing the hydrogenation activity of MnN_4 sites. We further calculate the C4—C5 bond strength of tetralin adsorbed on MnN_4@CNT(8, 8) compared with other systems (Table S5), and find a superior cracking performance on MnN_4@CNT(8, 8). Figure S15 displays the optimized structures after the C4—C5 bond cleavage for all the configurations with different curvatures. These results collectively indicate that MnN_4@CNT(8, 8) exhibits the best catalytic performance for naphthalene hydrocracking among the five systems studied. As shown in Figure S16, the *d*-band center exhibits curvature-dependence, the highest d-band center (–0.789 eV) is for MnN_4@CNT(8, 8) exhibits, lying closest to the Fermi level among the series. This alignment optimally strengthens substrate–adsorbate interactions, stabilizes the transition states for both hydrogenation and C—C cleavage, and thus yields the lowest energy barriers.

3 | Conclusions

In summary, we propose the utilization of single-metal-atom chains as highly efficient catalysts for heavy oil hydrocracking. Based on systematic first-principles calculations and rational screening, we have identified MnN_4@CNT(8, 8) as an optimal candidate that exhibits both superior hydrogenation and cracking activities. We have further studied the reaction mechanisms and main products of naphthalene during the hydrocracking process on the MnN_4@CNT(8, 8) catalyst. The optimal reaction pathway for the hydrogenation of naphthalene to tetralin is identified as $1\alpha \rightarrow 4\alpha \rightarrow 2\beta \rightarrow 3\beta$ with the fourth one as the rate-determining step, requiring an activation energy of 1.47 eV. This pathway not only has energetic favorability but also preserves the symmetry of the reactant system. The subsequent cracking process of tetralin involves C—C bond cleavage, isomerization, and ring-opening. The resulting main products are O-Xylene, ethylene, and ethane, aligning with experimental observations for the BTEX family. Our findings highlight the promise of single-metal-atom chains as superior catalysts for heavy oil hydrocracking, encouraging future experimental exploration of such catalysts for industrial petrochemical applications.

4 | Computational Methods

Our calculations are performed by using the Vienna ab initio simulations package (VASP) [26, 27] based on density functional theory, where the projector augmented wave method [28] is used for describing the interaction between valence electrons and ion cores, and the plane waves with an energy cutoff of 500 eV are used to expand the electron wave functions. The exchange–correlation interaction among the valence electrons is treated with the Perdew–Burke–Ernzerhof (PBE) functional [29] within the generalized gradient approximation [30]. The vacuum space of 30 Å is adopted to avoid the interactions between the adjacent cells. A $1 \times 1 \times 6$ supercell is used for the catalytic models. To verify the adequacy of this supercell size, we test the adsorption energy of naphthalene, which is found to be well-converged, as shown in Table S6. Furthermore, the stable adsorption configurations of naphthalene on MnN_4@CNT(8, 8) with different supercell sizes are compared in Figure S17, demonstrating the reliability of the chosen model in eliminating spurious periodic–image interactions. The convergence thresholds of 10^{-4} eV and 10^{-2} eV Å^{-1} are set for the total energy and force, respectively. The Brillouin zone is represented by using $1 \times 1 \times 3$ Monkhorst-Pack *k*-meshes. Ab initio molecular dynamics (AIMD) simulations for these systems using their $1 \times 1 \times 8$ supercells are performed using the canonical ensemble with a Nosé–Hoover thermostat [31]. The climbing-image nudged elastic band (CI-NEB) method is used to obtain the energy barrier of transition states [32]. The bonding strength is measured with the integration of the bonding and antibonding states between neighboring atoms by projecting the corresponding crystal orbital Hamilton population (COHP) [33] as coded in the Lobster program [34]. To study the adsorption and interactions of molecules, the effect of van der Waals interactions is considered by using the PBE-D2 functional that contains the semi-empirical long-range dispersion correction [35]. The adsorption energy $E_{adsorption}$ is calculated based on the following equation defined as: $Eadsorption = Etotal - Esubstrate - Emolecule$, where, E_{total} represents the total energy of the system, $E_{substrate}$ and $E_{molecule}$ refers to the single-point energies of the catalyst substrate and adsorbed molecules, respectively. The formation energy (E_f) of the $Mn_xN_y@C_z$ system is calculated to evaluate its thermodynamic stability, defined as: $E_f = (E_{MnxNy@Cz} - xE\text{Mn s} - yE\text{N s} - zE\text{C s})/(x+y+z)$, where $E_{MnxNy@Cz}$ is the total energy of the composite system, *E*Mn s, *E*N s, and *E*C s represent the energy of each Mn, N, and C atom in its most stable bulk phase, respectively.

25130390, 2026, 3, Downloaded from https://advanced.onlinelibrary.wiley.com/doi/10.1002/adts.202501713 by Peking University, Wiley Online Library on [03/04/2026]. See the Terms and Conditions (https://onlinelibrary.wiley.com/terms-and-conditions) on Wiley Online Library for rules of use; OA articles are governed by the applicable Creative Commons License

Acknowledgements

This work was supported by the China National Petroleum Corporation-Peking University Strategic Cooperation Project of Fundamental Research andNational Natural Science Foundation of China (Grant No. NSFC-12274007). It was also supported by the high-performance computing platform of Peking University, China.

Conflicts of Interest

The authors declare no conflicts of interest.

Data Availability Statement

The data that support the findings of this study are available from the corresponding author upon reasonable request.

References

1. M. S. Rana, V. Sámano, J. Ancheyta, and J. A. I. Diaz, "A Review of Recent Advances on Process Technologies for Upgrading of Heavy Oils and Residua," *Fuel* 86 (2007): 1216–1231.

2. A. Kostyniuk, D. Bajec, and B. Likozar, "Catalytic Hydrocracking Reactions of Tetralin as Aromatic Biomass Tar Model Compound to Benzene/Toluene/Xylenes (BTX) Over Zeolites Under Ambient Pressure Conditions," *Journal of Industrial and Engineering Chemistry* 96 (2021): 130–143.

3. D. Lašič Jurković, A. Kostyniuk, and B. Likozar, "Mechanisms, Reaction Micro-Kinetics and Modelling of Hydrocracking of Aromatic Biomass Tar Model Compounds into Benzene, Toluene and Xylenes (BTX) over H-ZSM-5 Catalyst," *Chemical Engineering Journal* 445 (2022): 136898.

4. W. Zhao, H. Yu, S. Peng, W. Liu, W. Zhang, and D. Mei, "Mechanistic Understanding of Anthracene Hydrocracking Over HY Zeolite Encapsulated Single-Atom Pt Catalysts," *ACS Catalysis* 14 (2024): 8836–8855.

5. M. A. Arribas, A. Corma, M. J. Díaz-Cabañas, and A. Martínez, "Hydrogenation and Ring Opening of Tetralin Over Bifunctional Catalysts Based on the New ITQ-21 Zeolite," *Applied Catalysis A: General* 273 (2004): 277–286.

6. A. T. Townsend and J. Abbot, "Catalytic Cracking of Tetralin on HY Zeolite," *Applied Catalysis A: General* 90 (1992): 97–115.

7. J. Weitkamp, "Catalytic Hydrocracking—Mechanisms and Versatility of the Process," *Chemcatchem* 4 (2012): 292–306.

8. T. Pan, S. Ge, M. Yu, et al., "Synthesis and Consequence of Zn Modified ZSM-5 Zeolite Supported Ni Catalyst for Catalytic Aromatization of Olefin/Paraffin," *Fuel* 311 (2022): 122629.

9. M. Marinescu, D. R. Popovici, D. Bombos, et al., "Hydrodeoxygenation and Hydrocracking of Oxygenated Compounds Over CuPd/γ-Al2O3–ZSM-5 Catalyst," *Reaction Kinetics, Mechanisms and Catalysis* 133 (2021): 1013–1026.

10. C. Mu, J. Sun, C. Xie, et al., "Shape Selectivity of AEL Channels for Anomalously Facilitating Biojet Fuel Production From Long-Chain n - Alkane Hydrocracking," *ACS Catalysis* 14 (2024): 1394–1404.

11. R. Kumar Parsapur, A. M. Hengne, G. Melinte, et al., "Post-Synthetic Ensembling Design of Hierarchically Ordered FAU-type Zeolite Frameworks for Vacuum Gas Oil Hydrocracking," *Angewandte Chemie* 136 (2024): 202314217.

12. P. Liu, Y. Zhao, R. Qin, et al., "Photochemical Route for Synthesizing Atomically Dispersed Palladium Catalysts," *Science* 352 (2016): 797–800.

13. X. Wang, W. Chen, L. Zhang, et al., "Uncoordinated Amine Groups of Metal–Organic Frameworks to Anchor Single Ru Sites as Chemoselective Catalysts Toward the Hydrogenation of Quinoline," *Journal of the American Chemical Society* 139 (2017): 9419–9422.

14. J. Li, W. Xia, J. Tang, et al., "Metal–Organic Framework-Derived Graphene Mesh: A Robust Scaffold for Highly Exposed Fe–N_4 Active Sites Toward an Excellent Oxygen Reduction Catalyst in Acid Media," *Journal of the American Chemical Society* 144 (2022): 9280–9291.

15. Y. Wang, H. Su, Y. He, et al., "Advanced Electrocatalysts With Single-Metal-Atom Active Sites," *Chemical Reviews* 120 (2020): 12217–12314.

16. B. Lu, Q. Liu, and S. Chen, "Electrocatalysis of Single-Atom Sites: Impacts of Atomic Coordination," *ACS Catalysis* 10 (2020): 7584–7618.

17. C. Manrique, A. Guzmán, J. Pérez-Pariente, C. Márquez-Álvarez, and A. Echavarría, "Vacuum Gas-Oil Hydrocracking Performance of Beta Zeolite Obtained by Hydrothermal Synthesis using Carbon Nanotubes as Mesoporous Template," *Fuel* 182 (2016): 236–247.

18. G. Sun, D. Liu, M. Li, et al., "Atomic Coordination Structural Dynamic Evolution of Single-Atom Mo Catalyst for Promoting H_2 Activation in Slurry Phase Hydrocracking," *Science Bulletin* 68 (2023): 503–515.

19. G. Sun, D. Liu, H. Shi, et al., "Oxygen-Vacancy-Induced Built-In Electric Field Across MoCo Dual-Atomic Site Catalyst for Promoting Hydrogen Spillover in Hydrocracking and Hydrodesulfurization," *ACS Catalysis* 14 (2024): 3208–3217.

20. W. Qin, S. Guo, Z. Liu, et al., "Coherently Confined Single-Metal-Atom Chains in 2D Semiconductors," *Nature Communications* 16 (2025): 4924.

21. W. An and C. H. Turner, "Transition-Metal Strings Templated on Boron-Doped Carbon Nanotubes: A DFT Investigation," *The Journal of Physical Chemistry C* 113 (2009): 15346–15354.

22. Z. He, J. Zhou, X. Lu, and B. Corry, "Ice-Like Water Structure in Carbon Nanotube (8,8) Induces Cationic Hydration Enhancement," *The Journal of Physical Chemistry C* 117 (2013): 11412–11420.

23. G. Henkelman, A. Arnaldsson, and H. Jónsson, "A Fast and Robust Algorithm for Bader Decomposition of Charge Density," *Computational Materials Science* 36 (2006): 354–360.

24. W. Tang, E. Sanville, and G. Henkelman, "A Grid-Based Bader Analysis Algorithm Without Lattice Bias," *Journal of Physics: Condensed Matter* 21 (2009): 084204.

25. M. A. Spackman and P. G. Byrom, "A Novel Definition of a Molecule in a Crystal," *Chemical Physics Letters* 267 (1997): 215–220.

26. G. Kresse and J. Furthmüller, "Efficient Iterative Schemes for ab Initio Total-Energy Calculations using a Plane-Wave Basis Set," *Physical Review B* 54 (1996): 11169.

27. G. Kresse and J. Furthmüller, "Efficiency of ab-Initio Total Energy Calculations for Metals and Semiconductors Using a Plane-Wave Basis Set," *Computational Materials Science* 6 (1996): 15–50.

28. P. E. Blöchl, "Projector Augmented-Wave Method," *Physical Review B* 50 (1994): 17953–17979.

29. J. P. Perdew, K. Burke, and M. Ernzerhof, "Generalized Gradient Approximation Made Simple," *Physical Review Letters* 77 (1996): 3865.

30. M. P. Teter, M. C. Payne, and D. C. Allan, "Solution of Schrödinger's Equation for Large Systems," *Physical Review B* 40 (1989): 12255.

31. S. Nosé, "A Unified Formulation of the Constant Temperature Molecular Dynamics Methods," *Journal of Chemical Physics* 81 (1984): 511–519.

32. G. Mills and H. Jónsson, "Quantum and Thermal Effects in H2 Dissociative Adsorption: Evaluation of Free Energy Barriers in Multidimensional Quantum Systems," *Physical Review Letters* 72 (1994): 1124.

33. V. L. Deringer, A. L. Tchougréeff, and R. Dronskowski, "Crystal Orbital Hamilton Population (COHP) Analysis As Projected From Plane-Wave Basis Sets," *The Journal of Physical Chemistry A* 115 (2011): 5461–5466.

34. R. Nelson, C. Ertural, J. George, V. L. Deringer, G. Hautier, and R. Dronskowski, "LOBSTER: Local Orbital Projections, Atomic Charges, and Chemical-Bonding Analysis From Projector-Augmented-Wave-Based Density-Functional Theory," *Journal of Computational Chemistry* 41 (2020): 1931–1940.

25130390, 2026, 3, Downloaded from https://advanced.onlinelibrary.wiley.com/doi/10.1002/adts.202501713 by Peking University, Wiley Online Library on [03/04/2026]. See the Terms and Conditions (https://onlinelibrary.wiley.com/terms-and-conditions) on Wiley Online Library for rules of use; OA articles are governed by the applicable Creative Commons License

35. T. Bučko, J. Hafner, S. Lebègue, and J. G. Ángyán, "Improved Description of the Structure of Molecular and Layered Crystals: Ab Initio DFT Calculations with van der Waals Corrections," *Journal of Physical Chemistry A* 114 (2010): 11814–11824.

Supporting Information

Additional supporting information can be found online in the Supporting Information section.

Supporting file: adts70279-sup-0001-SuppMat.docx

25130390, 2026, 3, Downloaded from https://advanced.onlinelibrary.wiley.com/doi/10.1002/adts.202501713 by Peking University, Wiley Online Library on [03/04/2026]. See the Terms and Conditions (https://onlinelibrary.wiley.com/terms-and-conditions) on Wiley Online Library for rules of use; OA articles are governed by the applicable Creative Commons License